

Dynamic core-electron-polarization effect on the high-order harmonic generation process from a quantum-trajectory perspective


Cam-Tu Le ^{1,2,*}, Cong Ngo,³ Ngoc-Loan Phan ⁴, DinhDuy Vu,⁴ and Van-Hoang Le ^{4,†}

¹Atomic Molecular and Optical Physics Research Group, Advanced Institute of Materials Science, Ton Duc Thang University, Ho Chi Minh City 72915, Vietnam

²Faculty of Applied Sciences, Ton Duc Thang University, Ho Chi Minh City 72915, Vietnam

³Department of Physics, University of Paderborn, 100 Warburger Street, D-33098 Paderborn, Germany

⁴Computational Physics Key Laboratory, Department of Physics, Ho Chi Minh City University of Education, 280 An Duong Vuong Street, Ward 4, District 5, Ho Chi Minh City 72711, Vietnam

 (Received 14 November 2022; revised 23 February 2023; accepted 7 March 2023; published 3 April 2023)

It is argued that the dynamic core-electron polarization (DCEP) in polar molecules primarily affects harmonic processes at the ionization step only. This manifestation can also be understood in view of the strong-field assumption that the parent ion's potential becomes irrelevant when the electron is accelerated in the continuum-energy region. However, the scenario becomes vastly different, especially in the case of long-wavelength lasers as shown in this paper, where we demonstrate a complete physical picture of the DCEP on the harmonic process from asymmetric carbon monoxide (CO) molecules comprising the propagation step. To do so, we develop a visualization method for the harmonic process with and without DCEP based on Bohmian mechanics. As tracer particles evolving along quantum trajectories, Bohmian trajectories provide an intuitive picture of the harmonic process from the CO molecules. Remarkably, when the change of the harmonic intensity with respect to the DCEP inclusion cannot be explained by the instantaneous ionization rate, the Bohmian trajectories can attribute this change to the difference in the number of returning events and returning time of the electron after the propagation stage. By analyzing the dynamics of individual Bohmian trajectories (the acceleration and the time-frequency profile), we show that the DCEP alters nonlocally the innermost trajectories, which encode all the dynamics of the harmonic process. This insight into the DCEP effect necessitates a careful reinvestigation into other strong-field physics theories on the role of the target over the propagation stage.

DOI: [10.1103/PhysRevA.107.043103](https://doi.org/10.1103/PhysRevA.107.043103)

I. INTRODUCTION

When atoms or molecules are subjected to an intense ultrashort laser, they might emit high-frequency photons in a process called high-order harmonic generation (HHG) [1–3]. This is a frequency up-conversion process because a long-wavelength (e.g., near- or midinfrared) laser can generate a soft x-ray spectrum through the nonlinear response of the target [4,5]. Intuitively, this process can be separated into three sequential stages for a valence electron: (i) ionization, (ii) propagation, and (iii) recombination, which are described semiclassically in the three-step model [6,7] assuming the strong-field approximation. For more detail about the description that underlies most of the strong-field phenomena and its vast development and recent applications, see Ref. [8] and references therein. Going beyond the strong-field approximation, one can approach the problem through *ab initio* methods to obtain exact numerical wave functions for calculating HHG. However, directly solving the Schrödinger equation, the time-dependent Schrödinger equation (TDSE) method, is only feasible for one- and two-electron systems [9–17].

Nevertheless, the TDSE method combined with the single-active-electron (SAE) model for the multielectron potential has been successfully applied to many multielectron systems and reduces computational resources significantly [7,18–24].

In strong-field physics, it is widely accepted that only the electron of the highest occupied molecular orbitals interacts with the laser field and plays the dominant role. However, the multielectron effects are found to be important in some cases. Particularly in the last ten years, dynamic core-electron polarization (DCEP), a cation polarization induced by the laser, has been important in describing the strong-field processes of some multielectron systems, such as calcium (Ca) and argon (Ar) atoms [25,26], carbon monoxide (CO) [27–31], carbon dioxide (CO₂) [32,33], carbonyl sulfide (OCS) [34], and carbon disulfide (CS₂) [33] molecules. Moreover, we recently figured out that DCEP is not a correction term but plays an essential role for HHG from CO molecules [35]. In this case, DCEP modulates both the intensity and phase of harmonics, making the even-to-odd harmonic ratio more consistent with the experimental data [36,37].

In theoretical studies of HHG, DCEP's trace has just been revealed clearly in the “final” results—the high-energetic photon spectra. When carefully comparing the two scenarios with and without DCEP, the origin of the difference in the harmonic intensity is attributed to the ionization rate [28] or, more

*lethicamtu@tdtu.edu.vn

†hoanglv@hcmue.edu.vn

precisely, the instantaneous ionization rate at a specific ionization instant [30]. This result is expected because the electron movement in the continuum region is not much influenced by the parent ion Coulomb interaction as well established within the tunneling ionization regime [6,7,38–41]. However, this picture of the DCEP effect may be incomplete by not considering the effect of DCEP on the propagation phase, particularly under long-wavelength lasers.

If based on the well-known “ansatz” first proposed in Ref. [42], the harmonic intensity is factorized into the recombination dipole matrix element and a complex continuum electron-wave-packet amplitude. The latter factor encodes both the ionization and continuum electron-wave-packet acceleration. By measuring the HHG spectra from different noble gases, the authors of Ref. [39] showed that the complex continuum electron-wave-packet amplitude strongly depends on both the target ground-state energy and the laser pulse. This evidence can be easily understood based on the Ammosov-Delone-Krainov theory [43], where ionization depends only on the target ground-state energy and the laser intensity. Moreover, in the conventional strong-field approximation [6,7], the excursion in the continuum of electron wave packets is only governed by the laser field, ignoring the effect of the ion potential. However, it is known that the inclusion of the Coulomb potential may be inevitable in the strong-field processes [44,45]. Additionally, when taken into account, DCEP also causes a polarization potential [27,30,46] which may have a considerable and thus non-negligible impact in the propagation stage. Recently, exploiting the multiconfiguration time-dependent Hartree-Fock method [47], the authors have studied the multielectron dynamics of CO molecules in multicolor lasers. By analyzing temporal profiles of the configuration-interaction (CI) coefficients, the rising in intensity of some harmonics for the two-color laser is attributed to increase of the CI coefficient corresponding to the configuration of excitation from the ground-state configuration. Also, with specific laser parameters in that case, the excursion amplitude of the ionized electron is quite small (11 a.u.), indicating that the ion core effect on the liberated electron cannot be ignored.

Bohmian mechanics [48] is an alternative and complementary quantum approach for studying strong-field processes with an intuitive picture in terms of electron trajectories. Based on the concept of individual trajectories associated with the probability amplitude and their emission times, the Bohmian trajectory (BT) can complement the direct analysis of electron density obtained by the numerical TDSE method. By solving the guiding equation with wave functions extracted directly from the TDSE with the time-dependent laser field and fully integrated target ion binding potential, the BT has been exploited in various problems, such as HHG [49–52] and laser-driven electron dynamics [53–60]. Recently, the BT has also been used to explore HHG in solids [61], and the tunneling process in attoclock experiments [62]. Based on the well-defined trajectories in space and time, Bohmian mechanics can provide the electron dynamics during the ionization process [60] and can be used to justify the tunnel exit point from where a classical trajectory starts its excursion in the continuum region of a given model [62]. Regarding HHG, we believe that the BT is also a powerful tool to investigate the

origin of the DCEP effect on the harmonic process. However, this method has been implemented just for one-dimensional (1D) problems with a soft-Coulomb potential [49–51,53–56], a short-range Yukawa potential [60], or a Mathieu-type potential [61]. Therefore, we will first upgrade the BT method to be compatible with more complex asymmetric molecules and then adopt it for our purpose.

In this paper, we aim to visualize the effect of DCEP on the harmonic process of CO molecules by the dynamics of Bohmian trajectories. We especially focus on cases where the change of harmonic intensity is not correlated to that of the instantaneous ionization rate. This situation signifies the role of DCEP on the propagation phase, which is discussed in a few works in the literature, such as Ref. [47]. Furthermore, by analyzing the accelerations of individual trajectories and the ensembles thereof, we figure out the “central” trajectory, which can decode all harmonic processes’ dynamics under a specific set of laser parameters. Our study yields a complete picture of the DCEP effect incorporating the propagation step. This insight may challenge the premise that the DCEP contributes only to the ionization and recombination steps.

The rest of the paper is organized as follows. In Sec. II, we present the theoretical method, including solving the TDSE, getting the Bohmian trajectories, and obtaining the ionization and the harmonic spectra. In Sec. III, we show the results of an exemplified case where the DCEP manifests its effect in the propagation step. Then we unravel the underlying mechanism of the harmonic process through the dynamics of Bohmian trajectories. We finish our investigation in Sec. IV, in which we briefly summarize the main results obtained.

II. THEORETICAL METHOD

A. TDSE + SAE calculation

Using the traditional Bohmian scenario to analyze the strong-field process of a system in a laser field requires the electron wave functions; thus, the first task is to solve the TDSE describing the laser-matter interaction as

$$i \frac{\partial}{\partial t} \Psi(\mathbf{r}, t) = [\hat{H}_0(\mathbf{r}) + \hat{H}_{\text{int}}(\mathbf{r}, t)] \Psi(\mathbf{r}, t). \quad (1)$$

Here, $\hat{H}_0 = -\nabla^2/2 + V_{\text{SAE}}(\mathbf{r})$ is the field-free Hamiltonian of the system with the molecular potential $V_{\text{SAE}}(\mathbf{r})$ constructed using the single-active-electron potential model [21,22]. Without losing generality, we assume the CO molecule is perfectly oriented along the z axis, with the C atom placed at the positive and the O atom at the negative parts ($z_{\text{C}} = 1.215$ a.u. and $z_{\text{O}} = -0.917$ a.u.). Also, the ionization potential energy of the CO molecule should match the experimental value $I_p = -0.514$ a.u. given in Ref. [63], so we choose two empirical parameters of the LB α model [64] as $\alpha = 1.15$ and $\beta = 0.05$.

The second term on the right-hand side of Eq. (1) is $\hat{H}_{\text{int}}(\mathbf{r}, t) = V_{\text{L}}(\mathbf{r}, t) + V_{\text{P}}(\mathbf{r}, t)$ consisting of two parts: (i) the interaction potential between the active electron and the laser electric field $\mathbf{E}(t)$ in the length gauge $V_{\text{L}}(\mathbf{r}, t) = \mathbf{r} \cdot \mathbf{E}(t)$ and (ii) the polarization potential caused by the DCEP [27,46]:

$$V_{\text{P}}(\mathbf{r}, t) = -\frac{[\hat{\alpha}_c \mathbf{E}(t)] \cdot \mathbf{r}}{r^3}. \quad (2)$$

Because $V_P(\mathbf{r}, t)$ is divergent at the origin, the cutoff for $V_P(\mathbf{r}, t)$ is fulfilled at a position \mathbf{r}_c where the polarization field cancels the laser electric field, i.e., $V_P(\mathbf{r}_c, t) + V_L(\mathbf{r}_c, t) \approx 0$. When $\mathbf{r} \leq \mathbf{r}_c$, the electron is approximately field free [46]. In this paper, $\mathbf{E}(t)$ is linearly polarized in the yz plane and hereby makes an orientation angle θ with the molecular axis. The polarization response of a certain target ion in the laser field is characterized by its polarizability, $\hat{\alpha}_c$. For the CO molecule modeled as described above, the nonzero components of static polarizability of the core electrons are $\alpha_{cxx} = \alpha_{cyy} = 6.72$ and $\alpha_{czz} = 12.22$ taken from Ref. [29]. It should be noted that, using the DCEP, the results of ionization and HHG from the TDSE [29,30] are comparable to the full calculations from the time-dependent Hartree-Fock method [27,28] and the even-to-odd harmonic ratio [35] can match very well with the experiments [36,37]. These evidences indicate the static polarizability is accurate enough to describe the multielectron effect modeled by the DCEP. In fact, this is also sensible because the dynamic polarizability of CO^+ changes very slightly compared to the static polarizability. For example, in the case of 1000 nm, its components in the x (y) and z directions are increased by about 0.37 and 1.23%, respectively. With a longer wavelength (smaller frequency), the dynamic polarizability is very close to the static one.

We solve the Schrödinger equation (1) by the basis-set approach, expanding the time-dependent wave function $\Psi(\mathbf{r}, t)$ in terms of the eigenfunctions $\Phi_n^m(\mathbf{r})$ of the Hamiltonian \hat{H}_0 as

$$\Psi(\mathbf{r}, t) = \sum_{m=-\infty}^{\infty} \sum_{n=1}^{\infty} C_n^m(t) \Phi_n^m(\mathbf{r}). \quad (3)$$

Here, $C_n^m(t)$ are the time-dependent coefficients which can be obtained by the fourth-order Runge-Kutta scheme. In turn, the basis-set functions in spherical coordinates for a linear molecule $\Phi_n^m(\mathbf{r})$ are constructed by B-spline functions for the radial part [65] and spherical harmonics for the angular part [22,30].

Noting that because spurious transitions to the extraneous energy region may appear from the very high energy in the numerical calculation, which also significantly increases the computational overhead, the series by the quantum numbers of n and m in Eq. (3) is truncated at the value corresponding to the energy E_n^m , which is suitable for a certain strong-field process [65], such as harmonic generation or laser-induced electron diffraction [66,67]. Specifically, at the present stage, we consider the harmonics only at two opposite orientation angles: parallel and antiparallel to the laser polarization denoted as $\theta = 0^\circ$ and 180° . This consideration collapses the series of m to the initial value, $m = 0$. Therefore, the complete basis set is determined only by the series of n . Other simulation parameters are provided in the next section.

B. Bohmian trajectory

Bohmian mechanics is based on the idea that the dynamics of a particle is described by a set of trajectories whose evolution is described by a guiding wave function Ψ . Consequently, Bohmian trajectories are solutions of the guiding equation,

which reads as

$$\frac{d\mathbf{r}}{dt} = \text{Im} \frac{\nabla \Psi}{\Psi}. \quad (4)$$

From this equation, we can see that the Bohmian trajectory can be used to monitor the flow of probability density. To ensure the Bohmian trajectory correctly describes this flow, we use the traditional approach as in Refs. [49–52,54,55,57,58,60] based on the time-dependent wave function Ψ from the TDSE method given in Sec. II A. Because the particle trajectories are guided by the wave function, it means that one just needs to solve the above equation where the wave function (probability density) is nonzero.

Under the linearly polarized laser, the angular momentum projection onto the polarization direction of the laser field is conserved, meaning that the system will remain at the initial state of m . Particularly, in our case where $m = 0$, the wave function Ψ does not depend on the azimuthal angle φ anymore, and the gradient of the wave function is taken with respect to the radial distance r and polar angle ϑ only. Therefore, the dynamics equation of the BT is now equivalent to a set of three one-dimensional equations as follows:

$$\frac{dr}{dt} = \text{Im} \left(\frac{1}{\Psi} \frac{\partial \Psi}{\partial r} \right), \quad (5a)$$

$$\frac{d\vartheta}{dt} = -\frac{\sin \vartheta}{r^2} \text{Im} \left(\frac{1}{\Psi} \frac{\partial \Psi}{\partial \cos \vartheta} \right), \quad (5b)$$

$$\frac{d\varphi}{dt} = 0. \quad (5c)$$

We now solve Eqs. (5) for Bohmian trajectories. From Eq. (5c), we have $\varphi(t) = \text{const}$. Because the azimuthal angle φ does not change, the trajectories lie in the plane, consisting of the initial radius vector (at $t = t_0$) and the z axis. The set of coupled ordinary differential equations (5a) and (5b) can be solved numerically by the fourth-order Runge-Kutta algorithm.

The Bohmian trajectories are set to start from the rest, located around the atoms C and O. In principle, there are infinite trajectories. However, because we solve the equations on the grid, and the initial positions are considered as infinitesimal areas $\Omega_j(t_0)$, the number of trajectories is finite; thus, we need to weigh each trajectory based on the distribution function of the electronic probability density in the ground state $|\Psi(\mathbf{r}, t = t_0)|^2$. Each trajectory now has an associated weight w_j , which also determines the contribution of the j th trajectory to the harmonic spectrum. The value of the weight w_j can be calculated by generalizing the 1D formula in Ref. [54] to the two-dimensional case as

$$w_j = \int_{\Omega_j(t_0)} r^2 dr d(\cos \vartheta) |\psi(r, \cos \vartheta, t_0)|^2, \quad (6)$$

where $\psi = \Psi/\sqrt{2\pi}$ due to the symmetry of a linear molecule. Here, the infinitesimal area $\Omega_j(t_0)$ is given by

$$r_j(t_0) - \frac{\delta r_j}{2} < r < r_j(t_0) + \frac{\delta r_j}{2},$$

$$\vartheta_j(t_0) - \frac{\delta \vartheta_j}{2} < \vartheta < \vartheta_j(t_0) + \frac{\delta \vartheta_j}{2}.$$

C. Ionization rate and high-order harmonic spectrum

The instantaneous ionization rate can be calculated as in Ref. [68] by the formula

$$\Gamma(t) = -\frac{d[\ln P_b(t)]}{dt}, \quad (7)$$

where $P_b(t)$ is the survival probability at the bound states, $P_b(t) = \sum_{E_n^m < 0} |\langle \Phi_n^m(\mathbf{r}) | \Psi(\mathbf{r}, t) \rangle|^2$, with E_n^m being the energy values of the states Φ_n^m , i.e., the eigenvalues of the Hamiltonian \hat{H}_0 .

The intensity of a given harmonic order corresponding to frequency ω can be obtained by the Fourier transform as

$$H(\omega) = |\mathcal{F}\{a(t)\}|^2, \quad (8)$$

where

$$a(t) = \frac{d^2 \langle \Psi | z | \Psi \rangle}{dt^2} \quad (9)$$

is the dipole acceleration calculated from the expected value of the induced dipole $\langle z \rangle$. In the frame of Bohmian mechanics, the dipole acceleration is calculated by the formula $a(t) = \sum_j w_j a_{\text{BT}}^j(t)$, where

$$a_{\text{BT}}^j(t) = \frac{d^2 z_{\text{BT}}^j(t)}{dt^2} \quad (10)$$

is the acceleration of interested Bohmian trajectories $z_{\text{BT}}^j(t)$.

III. BOHMIAN-TRAJECTORY-BASED VISUALIZATION OF DCEP EFFECT ON HIGH-ORDER HARMONIC PROCESS

A. Case study of HHG intensity and ionization rate mismatch

First, we remind the reader that in our previous study [30] the DCEP's effect on the enhancement or suppression of HHG intensity in the cutoff region is ascribed to the enhancement or suppression of the instantaneous ionization rate around a specific instant t_i^* . When released at this instant, the electron can recombine and emit the photon with the highest frequency—the cutoff order. This result shows the predominant role of the ionization step of the DCEP effect on the harmonic process. However, in that study with a laser of 800 nm, the electron's excursion time is about 2.67 fs (110 a.u.), which may be relatively short to reveal the DCEP signature in the continuum-energy region. This guess inspires us to examine the universal property of the DCEP effect on the harmonic process of CO molecules by changing various laser parameters, such as the wavelength and number of optical cycles. As a result, we discover some cases and present in this section one case study in which the orientation angle is $\theta = 0^\circ$ and the laser parameters are chosen to exemplify the mismatch between the variation of interested harmonic-order intensity and the corresponding instantaneous ionization rate. We show that the DCEP in this case does not apparently affect the ionization rate at t_i^* , but the corresponding harmonic-order intensity—the cutoff intensity with DCEP is higher than that without DCEP.

We should note that the parameter $\gamma = \sqrt{2I_p} \omega_0 / E_0$ defined by Keldysh [38] is kept to 0.77 to ensure the harmonic process takes place with the same ionization mechanism when

varying the laser parameters. This value of the Keldysh parameter is the same as in our previous study [30], in which we figured out the correlation between the changes in ionization rate and harmonic intensity. The notations ω_0 and E_0 are respectively the frequency and peak amplitude of the laser pulse.

The electric field has the sine-squared envelope as

$$E(t) = E_0 \sin^2\left(\frac{\pi t}{\tau}\right) \sin(\omega_0 t + \phi), \quad (11)$$

with τ and ϕ being the time duration and carrier-envelope phase. To highlight the DCEP effect, we utilize the ultrashort pulse consisting of three optical cycles ($\tau = 3\tau_0$ where $\tau_0 = 2\pi/\omega_0$) and $\phi = -\pi/2$. The laser wavelength and intensity are respectively 1000 nm ($\omega_0 = 0.046$ a.u.) and 1.3×10^{14} W/cm² ($E_0 = 0.061$ a.u.) to remain $\gamma = 0.77$. With these laser parameters, we perform calculations within the simulation box of $R_{\text{max}} = 150$ a.u., which is more than five times the excursion amplitude of an electron moving in the laser electric field, $r_q = E_0/\omega_0^2$. To avoid the nonphysical reflection near the box edge, we apply the $\cos^{1/8}$ mask function [69] turning on from $r_{ab} = 120$ a.u. To construct the basis set for the wave function $\Psi(\mathbf{r}, t)$, we use 300 B-spline functions and 76 spherical harmonics. The series of n is expanded up to the states with energy about $17.5 U_p$, where the ponderomotive energy of the electron $U_p = E_0^2/(4\omega_0^2)$, and then the time-dependent wave function Eq. (3) is the expansion of 12 041 bases.

Within SAE and SAE plus DCEP (SAE + P), the HHG spectra in this section are obtained from the dipole acceleration Eq. (9), and the ionization rates are obtained from Eq. (7). The results are demonstrated in Fig. 1(a) showing that the harmonic cutoff ends at about the 43rd order (denoted as H43), which is in good agreement with the cutoff law $I_p + 3.17U_p$ [2,3,6,7]. Furthermore, the HHG intensity at around the cutoff (H43–H44) for the case with DCEP is about 4.8–5.36 times higher than that without DCEP. If the DCEP only affects the HHG intensity via the ionization rate at t_i^* as stated in the previous study [30], the enhancement of the HHG intensity in the cutoff region when including DCEP indicates that the ionization rate at t_i^* increases under effect of the DCEP. However, it is not the case as shown in Fig. 1(c).

To know $\Gamma(t_i^*)$, we first need to determine the instant t_i^* based on the kinetic-energy maps as a function of the ionization time by the electron trajectory concept given in Ref. [6]. Please note that, for more accuracy, an improved model, such as including the Coulomb potential [70,71], should be considered. It has been shown that the Coulomb-corrected ionization times are shifted to earlier values with the shift timescale in order of tens of attoseconds ($\approx 0.014\tau_0 - 0.023\tau_0$, where $\tau_0 \approx 2.67$ fs in these studies [70,71]). Thus, the estimation of ionization time from the classical model [6] is exact enough for the purpose of the present paper. From the obtained map (gray circles) shown in Fig. 1(b), one can determine the ionization instants corresponding to the recombination event which releases the photons in the cutoff region. Specifically, the ionization instants are around $t_i^* = 1.03\tau_0$, marked by the vertical dashed lines in Figs. 1(b) and 1(c). Figure 1(c) shows apparently that the ionization rate at t_i^* without DCEP equals that with DCEP. So, for the 1000-nm laser in the present paper, which drives the ionized electron in the continuum-energy

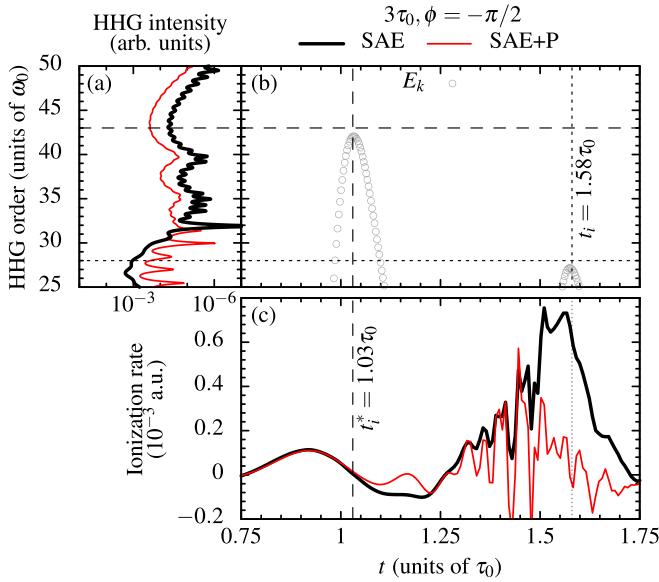


FIG. 1. HHG spectra (a) and ionization rates (c) of the CO molecule exposed to the laser pulse of 1000 nm, $\tau = 3\tau_0$, and $\phi = -\pi/2$ at $\theta = 0^\circ$. The results are obtained by solving numerically the TDSE within the single-active-electron framework (denoted as SAE by the thick black lines) and with the DCEP effect by adding the polarization potential Eq. (2) (denoted as SAE + P by the thin red lines) as Refs. [27,46]. For a clearer connection between the ionization instant and the emitted photon frequency, we plot the classical kinetic energy E_k as a function of time in panel (b). The vertical dashed lines mark the ionization instant $t_i^* = 1.03\tau_0$. If released at this instant t_i^* , the electron can emit (at recombination instant after returning) a photon with frequency marked by the horizontal dashed line. The vertical dotted lines specify the ionization instant $t_i = 1.58\tau_0$ that is responsible for a lower-frequency photon denoted by the horizontal dotted line.

region about 3.31 fs (137 a.u.), the ionization rates due to the effect of DCEP cannot fully explain the variation of the harmonic intensity. *It implies that the variation may come from the propagation step, which results in the different trajectories turning back the parent ion.*

To verify this, we will perform the Bohmian trajectories and present them in the next section. But before that, it is important to discuss briefly the ground that is also a qualitative explanation of our standpoint: the Newtonian form of a Bohmian particle evolving in time. If considering the law of motion for acceleration, one will get the *Bohm-Newton equation of motion*

$$\frac{d^2\mathbf{r}}{dt^2} = -\nabla[V_{\text{eff}}(\mathbf{r}, t) + Q(\mathbf{r}, t)], \quad (12)$$

with $V_{\text{eff}}(\mathbf{r}, t) = V_{\text{SAE}}(\mathbf{r}) + V_{\text{int}}(\mathbf{r}, t)$ being the classical potential, with $Q(\mathbf{r}, t) = -\frac{1}{2}\frac{\nabla^2 R}{R}$ being the quantum potential if the wave function is expressed as $\Psi(\mathbf{r}, t) = R(\mathbf{r}, t)e^{iS(\mathbf{r}, t)}$, with the amplitude R and phase S being real functions. Equation (12) is the equivalent version of the guiding equation [Eq. (4)] in case the constraint of initial momentum, $\mathbf{p}(t_0 = 0) = \nabla S(\mathbf{r}, t_0 = 0)|_{\mathbf{r}_0}$, is granted [48]. Regarding the initial positions, they are different from a classical model where the electron is prescribed classically by the Newton

equation after tunneling, so the initial position is assumed at the tunnel exit point that is classically expected at I_p/E_0 [38] or simply assumed approximately at the origin [6]. In Bohmian mechanics, the initial positions are distributed according to the probability density. When considering the DCEP effect, besides $V_L(\mathbf{r}, t)$, $V_{\text{int}}(\mathbf{r}, t)$ has the addition of $V_P(\mathbf{r}, t)$. Thus, the polarization potential affects the particle trajectory by entering explicitly into the equation and implicitly via the modification of the wave function in $Q(\mathbf{r}, t)$.

The Bohm-Newton equation implies that a long duration can amplify a small difference at initial time between the two cases: with and without $V_P(\mathbf{r}, t)$. It seems pretty weird because the excursion amplitude of the electron under longer wavelength is greater, while $V_P(\mathbf{r}, t)$ becomes smaller with larger distance (as the scale of $1/r^2$). However, the system starts evolving from the initial state with the electron distributing near the core (see in detail below) where the polarization potential is not small. So, the laser pulse with longer wavelength can drive the ionized electron for a longer propagation time, making the pathway difference between two model calculations manifest clearer.

B. Intuitive picture via Bohmian trajectories for DCEP effect: Predominant role of the propagation stage

Using Eqs. (5a), (5b), and (5c) with the time-dependent wave function obtained from numerically solving the TDSE, we launch an ensemble of 9440 trajectories with the initial positions ($t_0 = 0$) specified by 80 values of angle $\vartheta \in (0, \pi)$ and 118 values of $r \in [0.886, 15.0]$ a.u. It should be first mentioned that the meshes of r and ϑ variables are discretized nonuniformly by the Gaussian quadrature rule so that the meshes around the nuclei are densest. Then, we limit our consideration by this specific region of r because the weight w_j is diminutive (less than 10^{-12}) for $r(t_0 = 0) > 15.0$ a.u. Besides, for $r(t_0 = 0) < 0.886$ a.u., the electron just moves back and forth between the two nuclei [54] and does not contribute to the harmonic process. Moreover, when applying the cutoff for $V_P(\mathbf{r}, t)$, a portion of the trajectories starts from the region inside the cutoff point. If based on the confinement in configuration space, one may say that these trajectories would stay in bound states if their displacement is less than the exit point, which is classically expected at I_p/E_0 [38]. However, in quantum mechanics, we should study the dynamics of the HHG process through the dynamics—accelerations of individual Bohmian trajectories and ensembles thereof. For illustration, in Fig. 2, we present only 1280 trajectories with $r \in [1.556, 8.057]$ a.u., enough to demonstrate the general picture of our analysis. With this subset, one can still distinguish the individual trajectories with a large displacement in the two cases: SAE and SAE + P. As the number increases, the trajectories will become gradually a continuous grayscale. Concerning the lower value of the radial range, we do not show the trajectories with $r(t_0 = 0)$ smaller than this value because they do not give a spectrum with a well-defined cutoff.

As we can see in Fig. 2, subjected to the laser pulse whose period τ_0 also defines the time scale, the first ionized-electron bunch departs at around $1\tau_0$ toward the positive z direction, while the second bunch at around $1.5\tau_0$ moves toward the

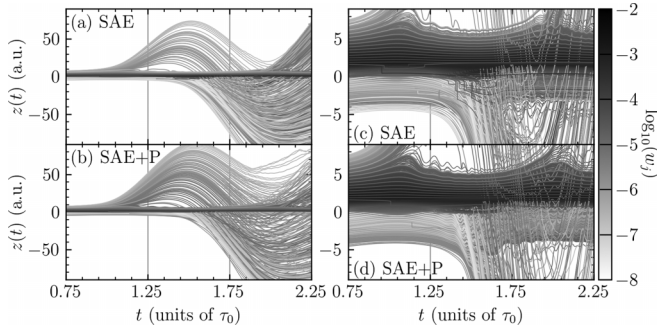


FIG. 2. Bohmian trajectories calculated with the time-dependent wave function obtained by the TDSE method within SAE (a) and SAE + P (b). The grayscale represents the weight of each trajectory in logarithmic scale, i.e., $\log_{10} w_j$. Panels (c) and (d) are the enlargement of the inner region close to the core.

negative z direction. When the laser electric field reverses its direction, the electron is driven backward. In general, each bunch can revisit the parent ion after about $0.3\tau_0$ – $0.7\tau_0$. This excursion time corresponds to the short electron trajectories in the electron concept proposed by Ref. [6]. From another side, Figs. 1(a) and 1(b) show that the electron ionized at around $t_i^* = 1.03\tau_0$ contributes to the harmonic intensity near the cutoff. In contrast, the electron ionized at around $t_i = 1.58\tau_0$ contributes to the harmonic intensity in the low-energy region. Therefore, with the purpose of exploring the origin of the HHG intensity variation in the cutoff region where the mismatch occurs, we are naturally interested in the dynamics of the first ionized-electron bunch only.

The Bohmian trajectories in Figs. 2(a) and 2(b) clearly show that the electron can revisit the parent ion with different pathways depending on whether the effective potential $V_{\text{eff}}(\mathbf{r}, t)$ includes the polarization term $V_P(\mathbf{r}, t)$ or not. Indeed, the number of trajectories with high weight (dark gray) returning around $t_r = 1.7\tau_0$ in Fig. 2(b) is visibly larger than that in Fig. 2(a). Specifically, by counting, the number of the Bohmian trajectories returning in the recombination time interval $1.6\tau_0$ – $1.8\tau_0$ in Fig. 2(b) is roughly twice more than that in Fig. 2(a). This can lead to the intensity of the harmonics emitted around $t_r = 1.7\tau_0$ when including DCEP being higher than that when ignoring DCEP regardless of the same ionization rate at $t_i^* = 1.03\tau_0$.

Besides the groups of Bohmian trajectories described above, a swarm of trajectories still localizes near the core ($|z| \lesssim 7$ a.u.), as depicted in Figs. 2(c) and 2(d). They are the so-called innermost trajectories. Accordingly, the trajectories making the excursion far away from the core ($|z| > 7$ a.u.) are called the outermost ones. As figured out in Ref. [51], the outermost trajectories will contribute to the overall HHG intensity, while the innermost trajectories define the structure of the harmonic spectra. It indicates that the larger the number of outermost trajectories is, the higher the HHG intensity is. So, in our case, with the larger number of peripheral trajectories, especially in the interval $t_r = 1.6\tau_0$ – $1.8\tau_0$, the HHG intensity in the cutoff region with the inclusion of DCEP is higher than without the DCEP.

More specifically, the number of the outermost trajectories in the first ionized-electron bunch is about 35 and 42% of the

total number of trajectories (4720 trajectories in the positive z axis) in the case of SAE and SAE + P, respectively. It means that visibly the DCEP effect causes about 7% difference in electron pathways that results in approximately twice more returning events responsible for the cutoff-energy region. This supports that the DCEP effect is mostly via the propagation step rather than the ionization one in this case. Up to this, intuitively and qualitatively, the general picture of Bohmian trajectories can explain the enhancement of HHG intensity when taking DCEP into account.

However, for more convincing evidence of the statement, we now discuss two things here. First, because the trajectories carry the weights, instead of the number of outermost (departure) trajectories or of returning (arrival) trajectories in a given time interval, we need to consider the numbers associated with w_j which are referred to as weighted numbers, $\mathcal{N} = \sum_j w_j$. Interestingly, the ratio of the weighted numbers of the returning trajectories in the time interval of $1.6\tau_0$ – $1.8\tau_0$ between SAE + P and SAE cases is about 5.0, which is very consistent with the ratio of the HHG intensity around the cutoff, 4.8–5.36. Meanwhile, the ratio of the weighted numbers of the outermost trajectories between SAE + P and SAE cases is about 4.33. It cannot fully explain the enhancement of HHG intensity around the cutoff of the SAE + P model. Second, it differs from the case of 800 nm [30], in which the ratios of the weighted numbers between SAE + P and SAE of the outermost trajectories and of the returning trajectories are respectively about 3.87 and 3.94. Both numbers can explain the enhancement of about four times HHG intensity around the cutoff (the 35th order). The nonidentical numbers in the case of 1000 nm (4.33 vs 5.0) indicate that the “arrangement” of the swarm of trajectories at the departure loses its order with a long evolution in time. In other words, these are the evidence of the DCEP effect on the propagation stage.

To complete our investigation, in the further analysis we show that the BT can reproduce quantitatively the HHG spectrum based on individual trajectories and the ensembles thereof. Due to the inherent nonlocality of the Bohmian trajectory—any changes in the flow of the wave function far from the core are transferred nonlocally to the inner region via the phase of the wave function [50,51]—the main feature of the HHG spectrum can be represented by innermost trajectories. So, we will discover the role of different Bohmian trajectories in the HHG spectrum in the next subsection.

C. Quantitative Bohmian trajectory analysis

For atoms, the central trajectory holding all essential information to obtain the HHG spectrum is the one with the initial position $z(t_0 = 0) = 0$, where the atoms are located [50,51]. In this sense, the central trajectories have yet to be shown for molecules, especially asymmetric ones. So, in this section, we first identify the central trajectories, which have a high contribution to the HHG spectrum and contain all the dynamic process information. In other words, the central trajectories should have the greatest weight and can reproduce the main feature of the harmonic spectrum from the TDSE. The role of other trajectories will then be uncovered through the buildup of ensembles of interested Bohmian trajectories

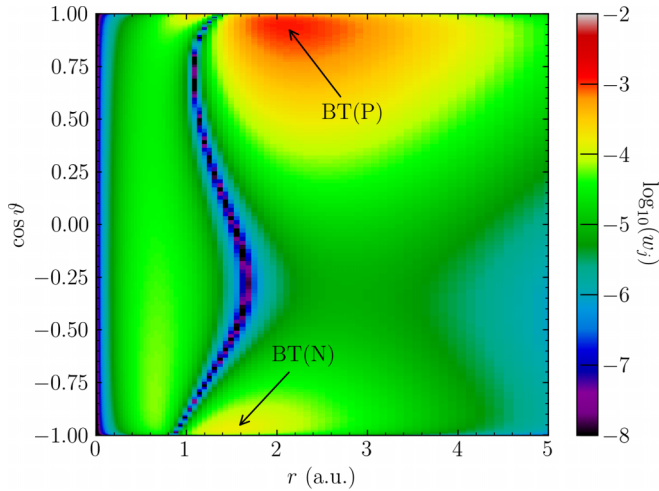


FIG. 3. Weights of the Bohmian trajectories in logarithmic scale, i.e., $\log_{10} w_j$. The arrows show two local maxima near the positions of C and O.

and time-frequency profiles. Along with these analyses, the nonlocality of the BT will be also evinced.

1. Central trajectories and the DCEP effect via electron propagation

To reveal *the central trajectory*, we scan the area surrounding the locations of C and O, which have the greatest probability of finding the electron. By thoroughly examining the frequency domain of BTs calculated by Eqs. (10) and (8), we realize that among the innermost BTs with initial positions (at $t_0 = 0$) surrounding the C's and O's locations, two trajectories are possible to encode all dynamic information of the harmonic process. The first one is the trajectory with $r = 2.106$ a.u. and $\cos \vartheta = 0.94$, near the C atom in the *positive* z axis, which is called BT(P). In the same manner, the second one is BT(N), denoted for the trajectory with $r = 1.556$ a.u. and $\cos \vartheta = -0.969$, near the O atom located in the *negative* part of the z axis. For illustration, we plot the calculated trajectory weights in Fig. 3 with indicated initial positions for the trajectories BT(P) and BT(N).

Plotted in Fig. 4(a), the two trajectories BT(P) and BT(N) oscillate in time with different frequencies and amplitudes upon including DCEP. We note that the weight of BT(N) is roughly one order of magnitude smaller than that of BT(P). However, we will compare their contributions to the HHG intensity below just by careful calculations besides looking at the weights.

To get insights into the high-order harmonic process and the DCEP impact, we will study the dynamics through *the acceleration of the Bohmian trajectory and its frequency domain*—the HHG spectrum. It is worth recalling that when looking into a dipole acceleration two features determine the main features of the HHG spectrum: (i) its oscillation period defining emitted photon frequency and (ii) its oscillation amplitude defining photon intensity.

We first look into the HHG dynamics through *the accelerations* of BTs(P) and BTs(N) calculated by Eq. (10) and shown in Figs. 4(b) and 4(c). For the first aspect, *the oscillation*

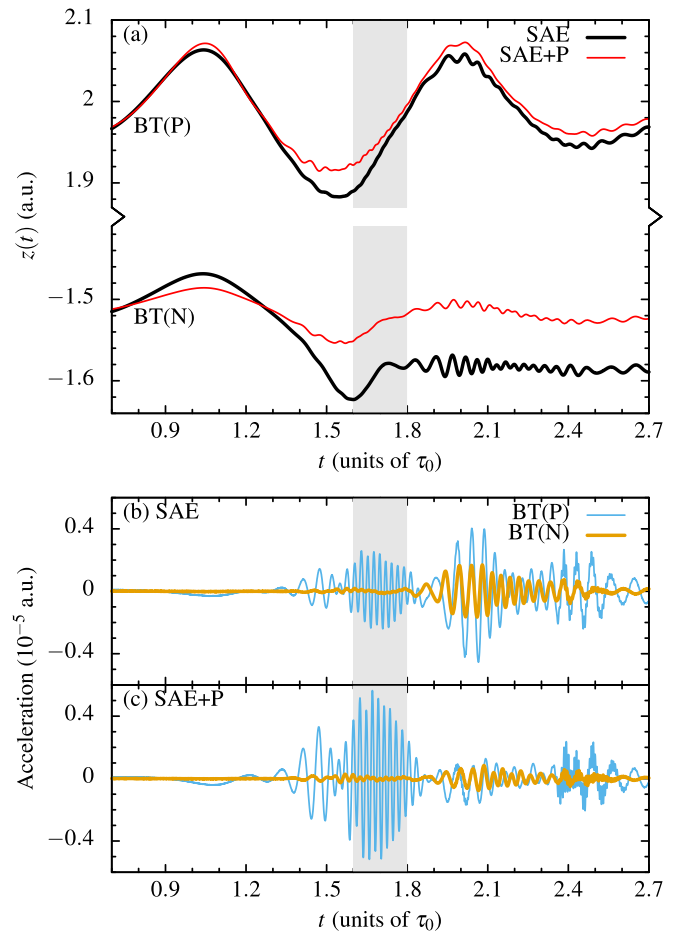


FIG. 4. (a) Bohmian trajectories with the initial positions near the C and O atoms, denoted as BT(P) and BT(N), respectively, obtained from the SAE (thick black lines) and SAE + P (thin red lines) models. (b, c) Acceleration of BT(P) (thin cyan lines) and BT(N) (thick orange lines) for SAE and SAE + P.

period, one can see that the accelerations for both BTs(P) (with and without DCEP) oscillate fast—high frequency—in the time interval of $1.6 \tau_0 - 1.8 \tau_0$, which is highlighted by the gray rectangles in Fig. 4. Within this time interval, the oscillations have the same period of $\tau_B \approx 0.023 \tau_0$ which corresponds to the frequency of $43 \omega_0$ —the cutoff order. Meanwhile, the accelerations of BTs(N) with relatively large amplitude oscillate within the time window $1.9 \tau_0 - 2.3 \tau_0$ slower with an oscillation period of about $\tau_B \approx 0.048 \tau_0 - 0.033 \tau_0$, which is responsible for the emitted low-energy photons in the frequency range of about $21 \omega_0 - 30 \omega_0$. Since we are interested in the cutoff region, we can ignore the contribution of BTs(N).

The above discussion for the trajectories in the innermost region is consistent with the intuitive picture given in Sec. III B for the outermost trajectories, visualized in Fig. 2. Indeed, the emitting time ($1.6 \tau_0 - 1.8 \tau_0$) of harmonics in the cutoff region from the innermost trajectories coincides with the returning time range of the majority of outermost trajectories in the first group. Also, the second ionized-electron group [BTs(N)] is ignored for both the outermost and innermost regions. It is evidence of the nonlocal property of the

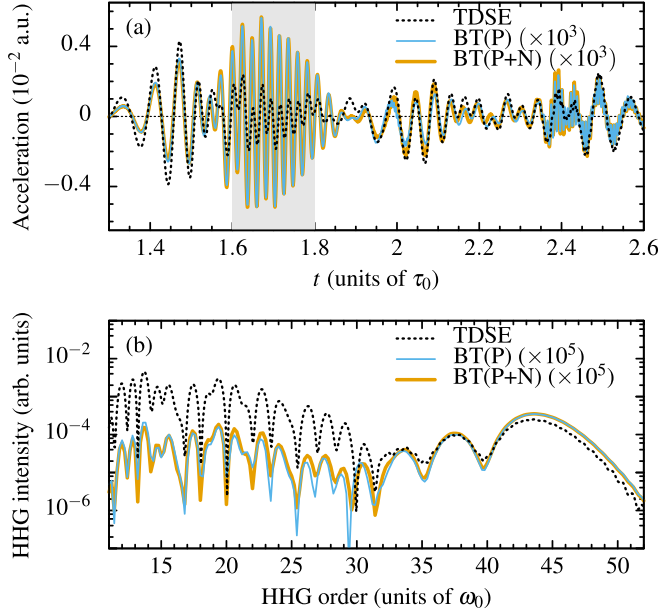


FIG. 5. Acceleration (a) and HHG (b) from the Bohmian trajectory with the maximum value of w_j , denoted as BT(P) (thin cyan lines), and from the sum of BT(P) and BT(N), denoted as BT(P+N) (thick orange lines) for the case of SAE + P. For convenience to compare, the results from the TDSE are plotted by the dotted black lines.

Bohmian trajectory: the innermost trajectories also contain the dynamics of the outermost trajectories. We will discuss the nonlocality of the BT in Sec. III C 3.

Turning to the second aspect of the acceleration, we can see that the *oscillation amplitudes* of BTs with DCEP differ from those without DCEP. Especially in the time interval of $1.6\tau_0$ – $1.8\tau_0$, where the acceleration oscillates fast (with $\tau_B \approx 0.023\tau_0$), the oscillation amplitude of SAE + P is higher than that of SAE. Consequently, the harmonic intensity in the cutoff region with DCEP is higher than that without DCEP. Therefore, from these analyses about oscillation period and amplitude, one can see that the dynamics—the acceleration—of BT(P) encodes the dynamic information of the process, and the role of DCEP occurring through electron propagation is apparent.

2. Representativeness of the central trajectories via the ensembles analysis

Besides the acceleration of the Bohmian trajectory, we move on to its frequency domain—the HHG spectrum to affirm the representative role of the central trajectory BT(P). Figure 5(a) presents the accelerations by Eq. (10) for three cases: (i) from the central trajectory BT(P) (thin cyan line), (ii) from the two trajectories BT(P) and BT(N), denoted as BT(P+N) (thick orange line), and (iii) from the TDSE calculation (dotted black line). One can see that the contribution of BT(N) only slightly corrects the oscillation amplitude of the acceleration of BT(P+N) in the time range of about $1.95\tau_0$ – $2.1\tau_0$, where the oscillation has a period of about $0.051\tau_0$ – $0.041\tau_0$. As a result, the calculation from the accelerations by Eq. (8) and shown in Fig. 5(b), the harmonic

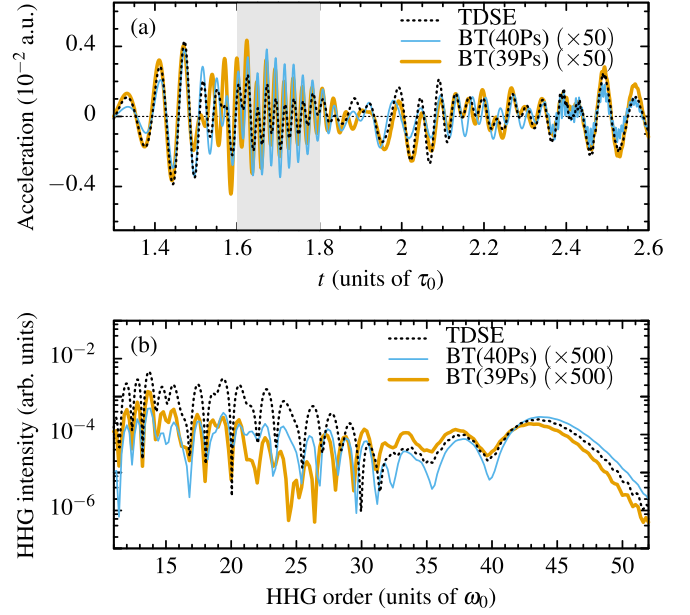


FIG. 6. Same as Fig. 5 but for two ensembles of 40 trajectories with $r = 2.106$ a.u. and $\cos\vartheta$ corresponding to $\vartheta \in (0^\circ, 90^\circ)$ at $t_0 = 0$ (thin cyan lines), and 39 trajectories with $\cos\vartheta = 0.94$ and $r \in [1.62, 5.0]$ a.u. at $t_0 = 0$ (thick orange lines).

spectrum from BT(P+N) is almost identical to that from BT(P) in the plateau region near the cutoff, larger than $35\omega_0$. In other words, the harmonic process mainly occurs at the C end, represented by the central trajectory BT(P).

Figure 5(b) also shows that the HHG spectrum from the central trajectory BT(P) has the same plateau structure (energy higher than $35\omega_0$) as that from the full TDSE calculation. We note that the representativeness of the central trajectory BT(P) is demonstrated here on the harmonic structure of the plateau region near the cutoff only but not the HHG intensity value, correct with the factor of $\approx 10^5$. Additionally, we consider the ensembles of trajectories around and including BT(P) and show the results in Fig. 6, for instance, the accelerations and HHG spectra for two cases: (i) 40 trajectories with initial positions at $r = 2.106$ a.u. and 40 values of $\cos\vartheta$ corresponding to $\vartheta \in (0^\circ, 90^\circ)$ and (ii) 39 trajectories with $\cos\vartheta = 0.94$ and 39 values of $r \in [1.62, 5.0]$ a.u. These cases are denoted as BT(40Ps) and BT(39Ps) and compared with the TDSE results. The figure shows that the harmonic spectra increase in intensity (with the multiplier factor of 500 to fit the HHG spectrum from the TDSE calculation) but maintain the harmonic structure near the cutoff as previous. The picture remains the same if including more innermost BTs(P) into the calculation but with the multiplier factor decreased, particularly equal to 1.78 when considering almost all innermost trajectories which have a typical harmonic structure with an apparent cutoff, about 2060 trajectories. These results support the idea of the central trajectory BT(P), meaning it keeps all dynamics of the harmonic process near the cutoff. To recover the full HHG plateau, including the low-energy region, we should consider more trajectories in the negative side of the z axis, i.e., BTs(N).

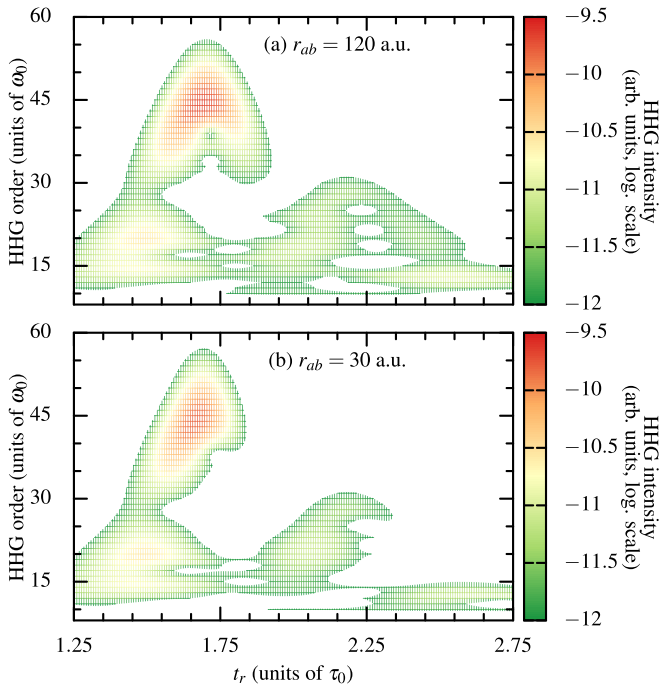


FIG. 7. Time-frequency profile of the acceleration of the BTs(P) in two cases: (a) $r_{ab} = 120$ a.u. and (b) $r_{ab} = 30$ a.u. illustrated for the case of SAE + P. The color code indicates the HHG intensity in logarithmic scale.

In this subsection, all calculations are performed for the case SAE + P. The results are similar for the SAE case because the representativeness of the central trajectory is common regardless of whether it is with DCEP or not (see the Appendix). Indeed, the harmonic intensity ratio at around the cutoff (H43–H44) from BT(P) in SAE + P and SAE is about 4.74, which is consistent with the ratio from the TDSE calculation (given the ratio of 4.8–5.36). This emphasizes the representativeness of the central trajectory BT(P).

3. Bohmian trajectory nonlocality

Now, we show other evidence of nonlocality of the BT by presenting the time-frequency profiles of the accelerations of BTs(P) obtained by Eq. (10), and illustrate for the case of SAE + P. For the SAE case, the physical picture is totally similar. To obtain the time-frequency map, we perform the Morlet wavelet transform [72,73] and exhibit the results in Fig. 7.

Figure 7(a) is the time-frequency map of BT(P) obtained when the time-dependent wave function is solved with $r_{ab} = 120$ a.u. One can see that although BT(P) localizes near the core, its time-frequency map reveals both short (left color arches) and long (right color arches) trajectories. In other words, the central trajectories can reflect the dynamics of the harmonic process. This result again emphasizes the central trajectory's role and leads to a natural question about the role of the outermost trajectories.

To address that question, we explore the time-frequency map of BT(P) when moving the absorption boundary from $r_{ab} = 120$ a.u. to near the excursion amplitude of the electron, $r_{ab} = 30$ a.u. $\approx r_q$, shown in Fig. 7(b). By doing that, the

long electron trajectories, whose excursion time is longer than $0.7\tau_0$, can be filtered out [74]. We can see that the time-frequency map in Fig. 7(b) now exhibits only the left color arches, i.e., only the retention of the short electron trajectories. Obviously, this illustrates that the change of the outermost trajectories, which results from the different probability density $|\Psi(\mathbf{r}, t)|^2$, transmits and alters nonlocally the innermost trajectories via the phase of the wave function [50,51].

Interestingly, calculated from the TDSE acceleration [Eq. (9)] when absorbing the long electron trajectories, the harmonic intensity at around the cutoff (H43–H44) decreases about 1.74–1.8 times. This is the nearly exact amount missed when considering only the innermost trajectories, 1.78, as given in the previous subsection. This result affirms that the outermost trajectories contribute nonlocally to the HHG intensity.

IV. CONCLUSION

In this paper, we first exemplify a case in which the DCEP effect manifests differently from the well-accepted mechanism at the ionization step. Then, using Bohmian trajectory analysis developed for three-dimensional linear molecules, we can explain qualitatively and quantitatively the effect of DCEP. Specifically, we show that the DCEP has nontrivial effect on the propagation stage, visibly increasing the number of returning events even though it does not affect the ionization step significantly. The result is an enhancement of HHG intensity near the cutoff compared to the computation without DCEP regardless of the same ionization rate in the two models.

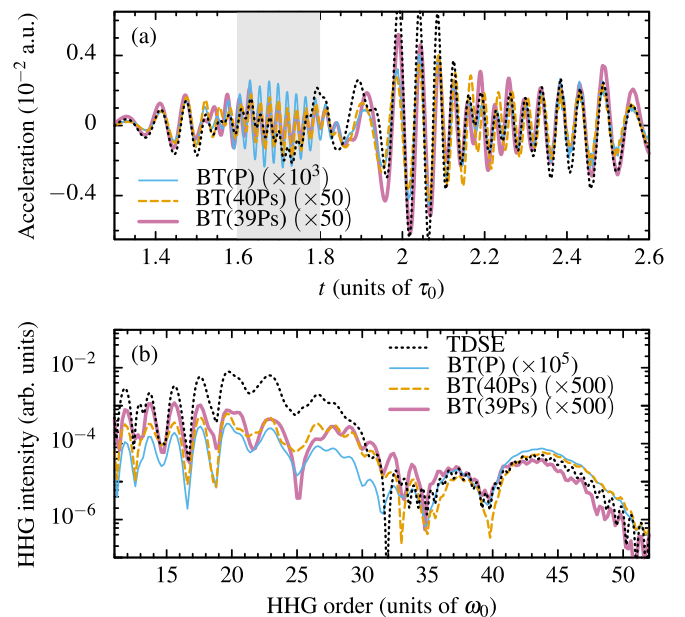


FIG. 8. Acceleration (a) and HHG (b) for the case of SAE from BT(P) with thin solid cyan lines, and from two ensembles as in Fig. 6: BT(40Ps) with dashed orange lines, and BT(39Ps) with thick solid pink lines. The results from the TDSE are plotted by the dotted black lines.

Furthermore, by tracing the dynamics of individual Bohmian trajectories, we identify the central trajectory holding all the dynamic information of the harmonic process in this case. The representativeness of this central trajectory can be clearly seen through the various ensembles of innermost Bohmian trajectories. Apart from that, the nonlocality of the Bohmian trajectory is also demonstrated through the time-frequency profile of the central trajectory.

We note that the wavelength of 1000 nm is the critical value where the mismatch between the instantaneous ionization rate and the corresponding HHG intensity starts to be revealed at some specific orientation angle such as $\theta = 0^\circ$. With longer wavelengths, such as 1600 nm (not shown) which results in longer time excursion, the manifestation of DCEP in the propagation step is more predominant.

ACKNOWLEDGMENTS

This work was funded by Vingroup and supported by Vingroup Innovation Foundation (VINIF) under project code

VINIF.2021.DA00031. The calculations were executed by the high-performance computing cluster at Ho Chi Minh City University of Education, Vietnam.

APPENDIX: ACCELERATIONS AND HHG SPECTRA FROM BOHMIAN TRAJECTORIES IN THE SAE CASE

In this Appendix, we present the acceleration and its Fourier transform—the HHG spectrum of the Bohmian trajectory guided by the wave function from the TDSE within SAE approximation.

By looking at the accelerations of BT(P), BT(40Ps), and BT(39Ps) and the corresponding HHG spectra shown in Fig. 8, one can see that, similar to the case of SAE + P in Sec. III C 2, BT(P) can reproduce the main features of the HHG spectrum, especially in the cutoff region. The larger ensembles are needed for the quantitative agreement in the low-energy region of the HHG.

-
- [1] A. McPherson, G. Gibson, H. Jara, U. Johann, T. S. Luk, I. A. McIntyre, K. Boyer, and C. K. Rhodes, *J. Opt. Soc. Am. B* **4**, 595 (1987).
- [2] J. L. Krause, K. J. Schafer, and K. C. Kulander, *Phys. Rev. A* **45**, 4998 (1992).
- [3] J. L. Krause, K. J. Schafer, and K. C. Kulander, *Phys. Rev. Lett.* **68**, 3535 (1992).
- [4] J. Seres, E. Seres, A. J. Verhoef, G. Tempea, C. Strelti, P. Wobrauschek, V. Yakovlev, A. Scrinzi, C. Spielmann, and F. Krausz, *Nature (London)* **433**, 596 (2005).
- [5] T. Popmintchev, M.-C. Chen, A. Bahabad, M. Gerrity, P. Sidorenko, O. Cohen, I. P. Christov, M. M. Murnane, and H. C. Kapteyn, *Proc. Natl. Acad. Sci. USA* **106**, 10516 (2009).
- [6] P. B. Corkum, *Phys. Rev. Lett.* **71**, 1994 (1993).
- [7] M. Lewenstein, P. Balcou, M. Y. Ivanov, A. L'Huillier, and P. B. Corkum, *Phys. Rev. A* **49**, 2117 (1994).
- [8] K. Amini, J. Biegert, F. Calegari, A. Chacón, M. F. Ciappina, A. Dauphin, D. K. Efimov, C. F. de Morisson Faria, K. Giergiel, P. Gniewek, A. S. Landsman, M. Lesiuk, M. Mandrysz, A. S. Maxwell, R. Moszyński, L. Ortmann, J. A. Pérez-Hernández, A. Picón, E. Pisanty, J. Prazdner-Bechcicki *et al.*, *Rep. Prog. Phys.* **82**, 116001 (2019).
- [9] M. Lein, N. Hay, R. Velotta, J. P. Marangos, and P. L. Knight, *Phys. Rev. Lett.* **88**, 183903 (2002).
- [10] G. Lagmago Kamta and A. D. Bandrauk, *Phys. Rev. A* **70**, 011404(R) (2004).
- [11] K.-J. Yuan and A. D. Bandrauk, *J. Phys. B: At. Mol. Opt. Phys.* **45**, 074001 (2012).
- [12] B. Fetić and D. B. Milošević, *Phys. Rev. E* **95**, 053309 (2017).
- [13] G. L. Kamta, A. D. Bandrauk, and P. B. Corkum, *J. Phys. B: At. Mol. Opt. Phys.* **38**, L339 (2005).
- [14] C. C. Chirilă and C. Chirilă, *Chem. Phys.* **366**, 54 (2009).
- [15] M. Awasthi, V. V. Yulian, and A. Saenz, *J. Phys. B: At. Mol. Opt. Phys.* **38**, 3973 (2005).
- [16] X. Guan, K. Bartschat, and B. I. Schneider, *Phys. Rev. A* **83**, 043403 (2011).
- [17] W.-C. Jiang, L.-Y. Peng, J.-W. Geng, and Q. Gong, *Phys. Rev. A* **88**, 063408 (2013).
- [18] E. Cormier and P. Lambropoulos, *J. Phys. B: At. Mol. Opt. Phys.* **30**, 3095 (1997).
- [19] I. A. Ivanov and A. S. Kheifets, *J. Phys. B: At. Mol. Opt. Phys.* **42**, 145601 (2009).
- [20] C. Vozzi, M. Negro, F. Calegari, G. Sansone, M. Nisoli, S. De Silvestri, and S. Stagira, *Nat. Phys.* **7**, 822 (2011).
- [21] M. Abu-samha and L. B. Madsen, *Phys. Rev. A* **81**, 033416 (2010).
- [22] S.-F. Zhao, C. Jin, A.-T. Le, T. F. Jiang, and C. D. Lin, *Phys. Rev. A* **81**, 033423 (2010).
- [23] S. Petretti, Y. V. Vanne, A. Saenz, A. Castro, and P. Decleva, *Phys. Rev. Lett.* **104**, 223001 (2010).
- [24] T.-Y. Du, Z. Guan, X.-X. Zhou, and X.-B. Bian, *Phys. Rev. A* **94**, 023419 (2016).
- [25] Z. Zhao and J. Yuan, *Phys. Rev. A* **89**, 023404 (2014).
- [26] A. A. Romanov, A. A. Silaev, M. V. Frolov, and N. V. Vvedenskii, *Phys. Rev. A* **101**, 013435 (2020).
- [27] B. Zhang, J. Yuan, and Z. Zhao, *Phys. Rev. Lett.* **111**, 163001 (2013).
- [28] B. Zhang, J. Yuan, and Z. Zhao, *Phys. Rev. A* **90**, 035402 (2014).
- [29] V.-H. Hoang, S.-F. Zhao, V.-H. Le, and A.-T. Le, *Phys. Rev. A* **95**, 023407 (2017).
- [30] C.-T. Le, V.-H. Hoang, L.-P. Tran, and V.-H. Le, *Phys. Rev. A* **97**, 043405 (2018).
- [31] M. Abu-samha and L. B. Madsen, *Phys. Rev. A* **101**, 013433 (2020).
- [32] C.-T. Le, D.-D. Vu, C. Ngo, and V.-H. Le, *Phys. Rev. A* **100**, 053418 (2019).
- [33] M. Abu-samha and L. B. Madsen, *Phys. Rev. A* **106**, 013117 (2022).
- [34] M. Abu-samha and L. B. Madsen, *Phys. Rev. A* **102**, 063111 (2020).

- [35] H. T. Nguyen, Kim-Ngan H. Nguyen, N.-L. Phan, C.-T. Le, D. D. Vu, L.-P. Tran, and V.-H. Le, *Phys. Rev. A* **105**, 023106 (2022).
- [36] E. Frumker, N. Kajumba, J. B. Bertrand, H. J. Wörner, C. T. Hebeisen, P. Hockett, M. Spanner, S. Patchkovskii, G. G. Paulus, D. M. Villeneuve, A. Naumov, and P. B. Corkum, *Phys. Rev. Lett.* **109**, 233904 (2012).
- [37] P. M. Kraus, D. Baykusheva, and H. J. Wörner, *Phys. Rev. Lett.* **113**, 023001 (2014).
- [38] L. Keldysh, *Sov. Phys. JETP* **20**, 1307 (1965).
- [39] J. Levesque, D. Zeidler, J. P. Marangos, P. B. Corkum, and D. M. Villeneuve, *Phys. Rev. Lett.* **98**, 183903 (2007).
- [40] X. Y. Lai, Q.-Y. Cai, and M. S. Zhan, *New J. Phys.* **11**, 113035 (2009).
- [41] X. Song, C. Lin, Z. Sheng, P. Liu, Z. Chen, W. Yang, S. Hu, C. D. Lin, and J. Chen, *Sci. Rep.* **6**, 28392 (2016).
- [42] J. Itatani, J. Levesque, D. Zeidler, H. Niikura, H. Pepin, J. C. Kieffer, P. B. Corkum, and D. M. Villeneuve, *Nature (London)* **432**, 867 (2004).
- [43] M. Ammosov, N. Delone, and V. Krainov, *Sov. Phys. JETP* **64**, 1191 (1986).
- [44] T. Brabec, M. Y. Ivanov, and P. B. Corkum, *Phys. Rev. A* **54**, R2551 (1996).
- [45] M. Klaiber, M. C. Kohler, K. Z. Hatsagortsyan, and C. H. Keitel, *Phys. Rev. A* **85**, 063829 (2012).
- [46] Z. Zhao and T. Brabec, *J. Mod. Opt.* **54**, 981 (2007).
- [47] S. Ohmura, H. Ohmura, T. Kato, S. Koseki, and H. Kono, *Chem. Phys. Lett.* **806**, 140045 (2022).
- [48] D. Bohm, *Phys. Rev.* **85**, 180 (1952).
- [49] Y. Song, F.-M. Guo, S.-Y. Li, J.-G. Chen, S.-L. Zeng, and Y.-J. Yang, *Phys. Rev. A* **86**, 033424 (2012).
- [50] J. Wu, B. B. Augstein, and C. Figueira de Morisson Faria, *Phys. Rev. A* **88**, 023415 (2013).
- [51] J. Wu, B. B. Augstein, and C. Figueira de Morisson Faria, *Phys. Rev. A* **88**, 063416 (2013).
- [52] H. Z. Jooya, D. A. Telnov, P.-C. Li, and S.-I. Chu, *J. Phys. B: At. Mol. Opt. Phys.* **48**, 195401 (2015).
- [53] P. Botheron and B. Pons, *Phys. Rev. A* **82**, 021404(R) (2010).
- [54] N. Takemoto and A. Becker, *J. Chem. Phys.* **134**, 074309 (2011).
- [55] S.-S. Wei, S.-Y. Li, F.-M. Guo, Y.-J. Yang, and B. Wang, *Phys. Rev. A* **87**, 063418 (2013).
- [56] R. Sawada, T. Sato, and K. L. Ishikawa, *Phys. Rev. A* **90**, 023404 (2014).
- [57] H. Z. Jooya, D. A. Telnov, P.-C. Li, and Shih-I Chu, *Phys. Rev. A* **91**, 063412 (2015).
- [58] H. Z. Jooya, D. A. Telnov, and S.-I. Chu, *Phys. Rev. A* **93**, 063405 (2016).
- [59] P.-C. Li, Y.-L. Sheu, H. Z. Jooya, X.-X. Zhou, and S.-I. Chu, *Sci. Rep.* **6**, 32763 (2016).
- [60] N. Douguet and K. Bartschat, *Phys. Rev. A* **97**, 013402 (2018).
- [61] X.-F. Pan, B. Li, T. Qi, J. Zhang, and X.-S. Liu, *J. Phys. B: At. Mol. Opt. Phys.* **54**, 025601 (2021).
- [62] W. Xie, M. Li, Y. Zhou, and P. Lu, *Phys. Rev. A* **105**, 013119 (2022).
- [63] K. Siegbahn, *J. Electron Spectros. Relat. Phenom.* **5**, 3 (1974).
- [64] R. van Leeuwen and E. J. Baerends, *Phys. Rev. A* **49**, 2421 (1994).
- [65] H. Bachau, E. Cormier, P. Decleva, J. E. Hansen, and F. Martín, *Rep. Prog. Phys.* **64**, 1815 (2001).
- [66] T. Zuo, A. Bandrauk, and P. Corkum, *Chem. Phys. Lett.* **259**, 313 (1996).
- [67] M. Meckel, D. Comtois, D. Zeidler, A. Staudte, D. Pavičić, H. C. Bandulet, H. Pépin, J. C. Kieffer, R. Dörner, D. M. Villeneuve, and P. B. Corkum, *Science* **320**, 1478 (2008).
- [68] D. A. Telnov, K. Nasiri Avanaki, and Shih-I Chu, *Phys. Rev. A* **90**, 043404 (2014).
- [69] H. Yu and A. D. Bandrauk, *Phys. Rev. A* **56**, 685 (1997).
- [70] L. Torlina and O. Smirnova, *New J. Phys.* **19**, 023012 (2017).
- [71] X. Xie, R. Xu, F. Zhang, S. Yu, X. Liu, W. Li, and Y. Chen, *J. Phys. B: At. Mol. Opt. Phys.* **55**, 185002 (2022).
- [72] P. Antoine, B. Piraux, and A. Maquet, *Phys. Rev. A* **51**, R1750 (1995).
- [73] X.-M. Tong and Shih-I Chu, *Phys. Rev. A* **61**, 021802(R) (2000).
- [74] M. Labeye, F. Risoud, C. Lévêque, J. Caillat, A. Maquet, T. Shaaran, P. Salières, and R. Taieb, *Phys. Rev. A* **99**, 013412 (2019).